Graphene Foam: Uniaxial Tension Behavior and Fracture Mode Based on a Mesoscopic Model

Douxing Pan,[†,‡,§,∥] Chao Wang,[‡,∥] Tzu-Chiang Wang,*[‡] and Yugui Yao*[†]

[†]Beijing Key Laboratory of Nanophotonics and Ultrafine Optoelectronic Systems, School of Physics, Beijing Institute of Technology, Beijing 100081, China

[‡]The State Key Laboratory of Nonlinear Mechanics, Institute of Mechanics, Chinese Academy of Sciences, Beijing 100190, China

[§]School of Engineering Science, University of Chinese Academy of Sciences, Beijing 100049, China

S *Supporting Information*

ABSTRACT: Because of the combined advantages of both porous materials and two-dimensional (2D) graphene sheets, superior mechanical properties of three-dimensional (3D) graphene foams have received much attention from material scientists and energy engineers. Here, a 2D mesoscopic graphene model (*Modell. Simul. Mater. Sci. Eng.* 2011, 19, 054003), was expanded into a 3D bonded graphene foam system by utilizing physical cross-links and van der Waals forces acting among different mesoscopic graphene flakes by considering the debonding behavior, to evaluate the uniaxial tension behavior and fracture mode based on *in situ* SEM tensile testing (*Carbon* 2015, 85, 299). We reasonably reproduced a multipeak stress−strain relationship including its obvious yielding plateau and a ductile fracture mode near 45° plane from the tensile direction including the corresponding fracture morphology. Then, a power scaling law of tensile elastic modulus with mass density and an anisotropic strain-dependent Poisson's ratio were both deduced. The mesoscopic physical mechanism of tensile deformation was clearly revealed through the local stress state and evolution of mesostructure. The fracture feature of bonded graphene foam and its thermodynamic state were directly navigated to the tearing pattern of mesoscopic graphene flakes. This study provides an effective way to understand the mesoscopic physical nature of 3D graphene foams, and hence it may contribute to the multiscale computations of micro/meso/macromechanical performances and optimal design of advanced graphene-foam-based materials.

KEYWORDS: *mesoscopic model, graphene foam, coarse-grained molecular dynamics, multipeak stress−strain curve, ductile fracture, power scaling law, multiscale physics−mechanics*
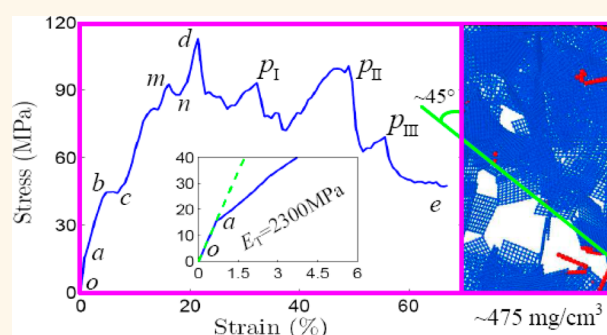
As a welcomed two-dimensional (2D) sheet, graphene is of great interest to both theorists and experimentalists owing to its ultrahigh intrinsic charge carrier mobility, large theoretical specific surface area, high modulus of elasticity, and thermal conductivity, as well as some interesting types of electronic properties such as Dirac point, Hall effect, and Berry's phase, as well as the topological insulator state and phase transition, which mainly arise from a host of quantum confinement effects and spin−orbit coupling characteristics.[1−4] Currently, as a reconstructed three-dimensional (3D) micro/nanoarchitecture,[5] graphene foam (GrF) with features of lightweight, high strength, and ultraflexibility serves as the key component in high-performance electrochemical energy storage and conversion devices such as lithium-ion batteries, supercapacitors, and fuel cells; it has been paid much attention in the material science and energy engineering fields.[6−8] Moreover, as a

biocompatible and conductive scaffold for the culturing of neural or human mesenchymal stem cells, GrF has already attracted attention in regenerative medicine owing to its directing differentiation, 3D porous structure, and electrical conductivity.[9,10]

Because of the combined advantages of both porous materials and 2D graphene sheets, much effort has been devoted to the development of effective and inexpensive processing technologies for fabricating high-performance 3D GrFs[5,11,12] such as all types of self-assemblies (so-called template-free methods), template-mediated methods, and other approaches including electrochemical synthesis and
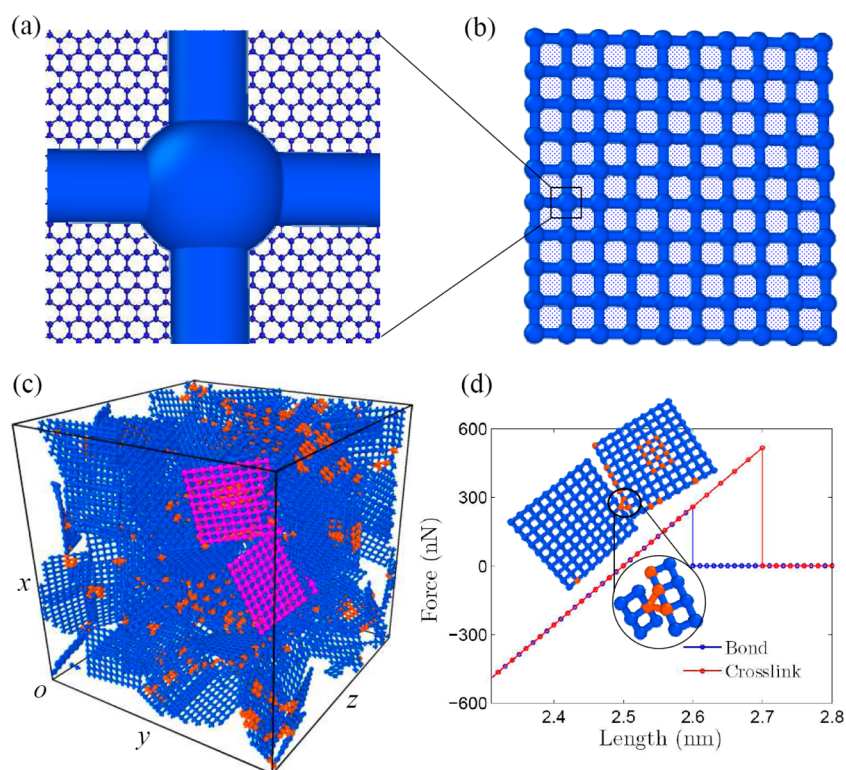
Figure 1. Schematics of 2D mesoscopic graphene model and 3D GrF numerical sample. (a) 2D mesoscopic graphene model for a bond-bead representative of 2.5 × 2.5 nm^2 planar section of single or multilayer graphene sheet.[23] (b) 2D mesoscopic graphene model for square mesoscopic lattice graphene flake composed of bond-beads for eight-layer graphene sheet. (c) Relaxed configuration of the 3D GrF numerical sample with physical cross-links (in red) and square flakes (in blue). (d) Force−length relationship used in the simulation for a single cross-link and bond (represented as red and blue sticks in the inset, respectively).

centrifugal evaporation-induced methods, as reviewed by Han *et al.*[6] and Fang *et al.*[13] Compared to the conventional counterparts such as rubbers or polyfoams, several different mechanical properties have been reported in succession, and as an important structural component, GrFs have been stealthily appealing to the eyes of researchers in the field of mechanics. For example, the material can sustain structural integrity under a load of >50,000 times its own weight[11] and can recover up to 98% compression in air and 90% in liquids between −196 and 900 °C.[14] They exhibit a combination of both cork-like and rubber-like properties, and Poisson's ratios in all directions are near-zero and largely strain-independent during giant reversible compression.[11,14,15] An approximate quadratic dependence of the compression modulus E_c on the foam's density ρ can be obtained, and a large range of tunable Poisson's ratios can be achieved by simply adjusting the prefreeze temperature.[11,14,15] The hyperelastic and/or viscoelastic and/or elastoplastic properties of their energy dissipation produced in compression are shown by the mechanical response of stress−strain hysteresis loops in cyclic loading−unloading experiments different from conventional rubber materials, and the storage and loss modulus as well as damping constant are insensitive to ambient temperature and loading frequency.[11,12,14,16] Recently, a series of tensile tests were carried out to evaluate the tensile properties and the corresponding multiscale deformation mechanisms of free-standing GrF[17] and GrF-related materials.[10,18,19] GrF-related materials mainly refer to polylactic acid−poly-ε-caprolactone copolymer (PLC) hybridization (GrF-PLC),[10] continuous graphene oxide porous fibers (GOPFs), and reduced graphene oxide porous fibers (RGPFs),[18] as well

as conductive unzipped or zipped carbon nanotube-based polydimethylsiloxane (GNR-PDMS, CNT-PDMS) composites.[19]

Comparatively speaking, few theoretical and/or computational studies have evaluated the constitutive relationship and corresponding intrinsic micro/nanostructural mechanisms of the above mechanical behaviors exhibited in experiments. Using full-atom molecular dynamic simulations, Baimova *et al.*[20] found that the nanostructures and mechanical properties of bulk amorphous carbon nanomaterials could be altered by shear deformation at a high temperature, leading to the formation of structural rearrangements that cannot be destroyed by further deformation and annealing, but extremely stable against diamondization (*i.e.*, no valence bonds with sp^3 hybridization) subject to hydrostatic compression without temperature dependence. Using the coarse-grained molecular dynamics method, Wang *et al.*[21] reproduced the rubber-like compressive constitutive behavior for complex 3D GrF materials in uniaxial compression, which consists of three typical stages consistent with the stress−strain response found in experiments,[11,14] and uncovered that Poisson's ratio can be effectively tuned by the stiffness of GrF flakes as well as the amplitude of external strains. Recently, Qin *et al.*[22] combined bottom-up computational modeling with experiments based on 3D-printed models and showed that the 3D graphene assembly has an exceptionally high ultimate tensile strength of 10 times as strong as mild steel at a relatively high density of 4.6% that of mild steel, but decreased with density much faster than those of polymer foams. In this study, a 2D mesoscopic graphene model developed by Cranford and Buehler[23] was expanded into 3D to
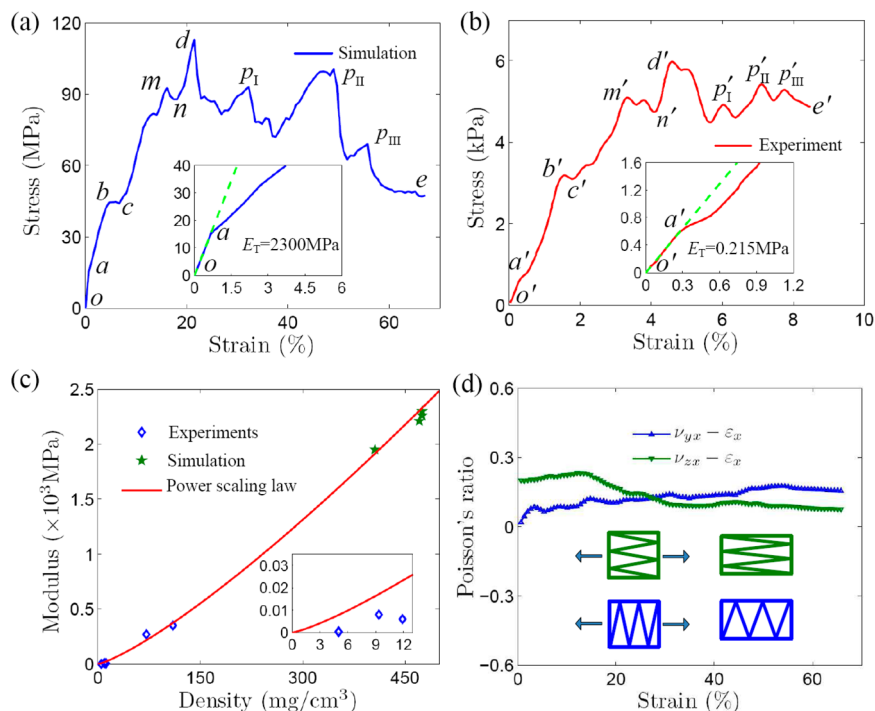
Figure 2. Uniaxial tension behaviors of 3D GrF and GrF-based materials. (a) Stress−strain curve in strain-controlled monotonic tensile loading based on the mesoscopic graphene model. (b) *In situ* SEM tensile testing curve reproduced from Nieto *et al.*[17] (c) Tensile elastic modulus as a power scaling law of mass density for 3D GrF,[17] GrF-PLC,[10] GOPF and RGPF,[18] and GNR-PDMS and CNT-PDMS[19] as well as GrF numerical samples. (d) Changes in Poisson's ratio with tensile strain and the corresponding mechanism sketches. The oa and $o'a'$ in the insets of (a,b) indicate proportional elastic lines, whose slopes are the modulus of elasticity.

evaluate the uniaxial tension behavior and fracture mode for a 3D GrF system based on the tensile experiment conducted by Nieto *et al.*[17] The mesoscopic model has already been applied to investigate the structure and conformational behavior of twisted ultralong multilayer graphene ribbons with a length of hundreds of nanometers, and a distinct transition from a saddle-like to coil-like configuration was observed, as a function of imposed rotation and number of graphene layers.[23] The rest of this article is organized as follows: First, the 2D graphene model is briefly introduced and subsequently expanded to a 3D GrF system by utilizing physical cross-links and van der Waals (vdW) forces acting among different graphene flakes by considering that the bead-bonds can be broken. On this basis, important mechanical behaviors of the GrF were reproduced, including the uniaxial tension constitutive relationship and ductile fracture mode near the 45° plane from tensile direction. Then, the internal multiscale rule of tensile elastic modulus with mass density was deduced, and the trend of Poisson's ratio with applied stress was determined. Finally, the physical mechanism of the tensile deformation through the evolution of mesostructure was elucidated, and a lively and direct view for the local rupture feature of the GrF was addressed. The conclusion and acknowledgments are given at the end of this paper.

RESULTS AND DISCUSSION

2D Mesoscopic Graphene Model. Based on the equivalent energy principle and a series of full atomistic calculations of a mechanical test suite, a 2D mesoscopic model for a sheet of graphene was established by Cranford and Buehler utilizing coarse-grain bead-spring elements with rotational-spring potentials.[23] In the 2D model, each bond-

bead represents a 2.5×2.5 nm^2 atomically single- or multilayer graphene sheet (Figure 1a). A harmonic spring potential:

$$\phi_T = k_T(r - r_0)^2/2 \qquad (1)$$

was used to describe the axial stretching energy among all pairs of bonded beads, where k_T is the spring constant and r is the distance between two beads with a referenced equilibrium distance r_0. A harmonic rotational-spring potential:

$$\phi_\varphi = k_\varphi(\varphi - \varphi_0)^2/2 \qquad (2)$$

was used to describe the in-plane bending energy under shear deformation, where k_φ is the spring constant related to the bending angle φ among the three bond-beads with a referenced equilibrium angle φ_0. Another harmonic rotational-spring potential:

$$\phi_\theta = k_\theta(\theta - \theta_0)^2/2 \qquad (3)$$

was used to describe the out-of-plane bending energy with a spring constant k_θ, where θ is the bending angle among the three bond-beads with a referenced value θ_0. The vdW interaction between different beads in an in-plane flake was described as a Lennard-Jones potential:

$$\phi_{LJ} = 4\varepsilon_{ip}[(\sigma_{ip}/r)^{12} - (\sigma_{ip}/r)^6] \qquad (4)$$

where ε_{ip} is an energy-scale parameter determining the depth of the potential well, σ_{ip} is a length-scale parameter that determines the position of the minimum potential, and r is the bead-to-bead distance in a cutoff range within the in-plane flake. The energy conservation between atomistic and mesoscale models was enforced to arrive at model parameters listed in Table S1 through elastic strain energy by incorporating

normal and shear strains, out-of-plane bending, and intra-molecular interactions.

3D Numerical Sample with Cross-Links. For a better application of the above 2D mesoscopic graphene model to investigate the mechanical properties and conformational features of 3D GrF, a huge cubic numerical sample comprising 125 coarse-grain graphene flakes was used as the initial geometrical configuration and each square flake with length of 25 nm as the building block containing 100 bond-beads as shown in Figure 1b. One flake in real materials contains 1−10 graphene layers;[6,10,13,17] therefore, 8 layers were adopted here. This can also approach the graphene branch in the *in situ* SEM sample very well,[17] where the 2D peak of the GrF Raman spectrum is 2726.1 cm^{-1}, comparable to the peak position of the GrF used by Chae *et al.*,[24] which indicates ~8−10 graphene layers. For simplicity, all the flakes in the numerical sample were assumed to be identical. Each coarse-grain graphene flake was strictly controlled by the 2D mesoscopic model, and the vdW interaction between particles situated in different neighboring coarse-grain flakes was described as a Lennard-Jones potential:

$$\phi_{LJ} = 4\varepsilon_{op}[(\sigma_{op}/r)^{12} - (\sigma_{op}/r)^{6}] \qquad (5)$$

where ε_{op} is the depth of the potential well, σ_{op} is the position of the minimum potential, and r is the distance between two beads among different graphene flakes in a cutoff range. The parameters were set as the same as that for beads situated inside the flake (Table S1), and the cutoff of Lennard-Jones potential was taken as 50 Å, above which the interactions between two particles tend to be insensitive to the distance.

In synthesis experiments, because of the squeezing effect or the covalent attachment of functional groups, the graphene sheets would form a monolithic chemically or physically linked 3D network.[11,14] Based on this fact, 3D linkages were also considered in our numerical GrF sample as labeled with red sticks in Figure 1c,d, and a cross-link model with a harmonic spring potential:

$$\phi_{cl} = k_{cl}(r - r_{cl})^2/2 \qquad (6)$$

was used to describe the 3D cross-links among different flakes, where k_{cl} is the spring constant and r is the distance between two beads situated in different neighboring coarse-grain flakes with a referenced equilibrium distance r_{cl}. The corresponding parameters were set to be the same as those for the bond in eq 1 listed in Table S1. Moreover, we assumed that the bond and cross-link would break when an ever-increasing tensile force is applied due to the fracture fact of the real GrF material.[17] The corresponding force−length relationships for a single cross-link and bond are shown in Figure 1d, where the angle and torsion energy of the cross-link are neglected for simplification, but the tensile strength of the cross-link was set to be higher than that of the bond in compensation.

Multipeak Uniaxial Tension Behavior. Figure 2a shows the stress−strain relationship in strain-controlled monotonic tensile loading for the 3D GrF with 721 cross-links based on the mesoscopic graphene model. This has a consistent trend as that for the *in situ* SEM tensile testing[17] reproduced in Figure 2b, although the mass density of our numerical sample is ~475 mg/cm^3, two orders larger than 5 mg/cm^3 of the real material. Moreover, as clearly shown in Figures 3, 5, and 6a below, a ductile fracture mode near 45° plane from tensile direction and its surface morphology together with an evolution of the local
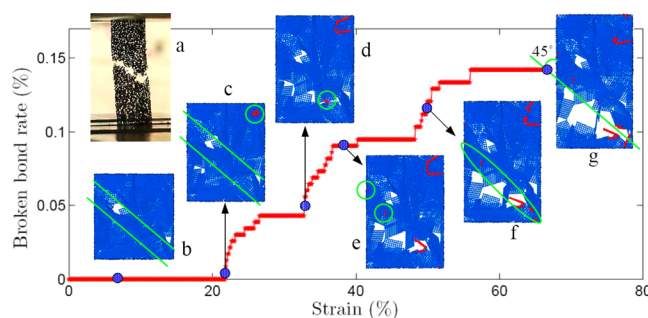
Figure 3. Fracture mode and the corresponding surface morphology of 3D GrF. The variation in the broken bond rate with the tensile strain based on the mesoscopic graphene model. The inset (a) shows the experimental sample reproduced from Nieto *et al.*,[17] and the insets (b−g) indicate the ductile fracture stages of the numerical sample (see Movie S1 in Supporting Information for the entire dynamic process). The flakes rearrange near a 45° plane from the tensile direction labeled by green lines, and the local broken bonds are highlighted by the connected red atoms and green circles or ellipse.

mesostructure in the numerical sample are all in good agreement with those observed in the experimental sample.[17] In Supporting Information, we provided a completely different GrF sample, where the number of cross-links is 830 with a density of ~471 mg/cm^3, and the resulting stress−strain curve and fracture mode shown in Figure S1 both coincide well with the current calculations. It is concluded that the 2D mesoscopic graphene model can be successfully expanded into the 3D GrF system, and the mechanical behaviors in the real GrF foam can be qualitatively described using the linkages and vdW potential among the neighboring graphene flakes. In the case of GrF shown in Figure 2a,b, the curves exhibit an elastic stage *ob* (*o'b'*), a yielding region *bc* (*b'c'*), followed by a hardening one *cd* (*c'd'*), and terminated with a fracture *de* (*d'e'*). In the elastic stage *ob* (*o'b'*) of the GrF, a defined proportional elasticity *oa* (*o'a'*) with elastic modulus of 2300 MPa (0.215 MPa) can be directly obtained from the insets of Figure 2a,b, and such a linear elastic behavior can also be observed in other graphene-related foams such as GrF-PLC,[10] GOPFs, and RGPFs,[18] as well as GNR-PDMS and CNT-PDMS.[19] Furthermore, we demonstrated that the deformation in the range of *ob* (*o'b'*) is mainly viscoelastic, where ~2.1% of viscous deformation is produced in the loading process, as shown in Figure S2a,b. Experimentally, GrF and GrF-based materials have been verified as viscoelastic materials through the storage and loss modulus as well as damping constant.[14,16]

In the case of compression, the compressive modulus E_c was found to scale with density ρ as $E_c \sim \rho^2$ for GrF-based materials.[14] Herein, based on the present numerical samples and existing tensile experiments (summarized in Table S1),[10,17−19] the relationship between tensile elastic modulus E_T [Notes: The reported modulus is the effective modulus of elasticity, because the GrF is a diphasic composite in which the phases (graphene and air) are connected in three dimensions.[31] The same reasoning is valid for the Poisson's ratio and ultimate tensile strength as well as such things] on the corresponding foam's density ρ was found to satisfy a simple power scaling law, that is,

$$E_T \sim 1.05\rho^{1.25} \qquad (7)$$

To examine the formula, only the linear elasticity of a large numerical sample with a density of ~406 mg/cm^3, containing 291.6 thousands of beads in a huge cubic box with a length of ~300 nm, was calculated due to the rapidly increasing computational complexity.[21] The obtained modulus is ~1950 MPa, which can also be approximately included in eq 7. Even so, as shown in Figure 2c, the power scaling curve still has an obvious mesoscale with a density region from 150 to 350 mg/cm^3 needing to be filled between the mesoscopic simulations and macroscale tensile experiments; therefore, more *in situ* SEM tensile tests of high-density GrFs are necessary to contribute to the above density region.

Figure 2d shows the nominal Poisson's ratios in both *y*-axis and *z*-axis directions as functions of tensile strain in the *x*-axis direction. In compressive experiments by recording movies, Wu *et al.*[14] showed a direction-independent and strain-invariant near-zero Poisson's ratio in GrF, and by simply adjusting the prefreeze temperature, Xu *et al.*[15] found that the naturally dried GrF exhibits a large range of tunable Poisson's ratio behavior, that is, $-0.3 < \nu < 0.46$. The optical images clearly showed three types of cross-section views, that is, vortex configurations ($\nu > 0$), laminated configurations ($\nu \approx 0$), and hyperbolic configurations ($\nu < 0$). Recently, using coarse-gained molecular dynamics simulations, Wang *et al.*[21] showed a series of isotropic strain-dependent Poisson's ratio with a feature of "U"-type variation trend during the uniaxial compression, varying from -0.1 to 0.8. This is consistent with the experiment of prefreeze temperatures below -60 °C.[15] However, here, Poisson's ratios in tensile simulations exhibit an anisotropic strain-dependent feature [Notes: All the materials, except some undergoing a certain phase transformation, exhibit a positive Poisson's ratio. Negative or near-zero Poisson's ratios can be, in principle, created by form factor engineering or by engineering the porosity in GrF or GrF-based materials. The deformation of GrF, whose magnitude will change with the applied stress, should affect the shape and then the effective Poisson's ratio (in this sense, it is strain-dependent for convenience). Hence, the Poisson's ratio is a shape effect arising from the structure of the GrF, and it is a property of the composite]. As shown in Figure 2d, with increasing tensile deformation, the Poisson's ratio ν_{yx} along the *y*-direction increased, whereas ν_{zx} along the *z*-direction slightly decreased. Such anisotropic Poisson's ratios ν_{yx} and ν_{zx} can be, at least partially, attributed to the "Z"-type and "N"-type percentage of disorder graphene flakes. This is because the former has enough space to shrink its lateral size in the beginning during the tensile deformation, while the latter at the end (see the schematic diagram in Figure 2d). For the simulated sample, the distribution of "N"-type along the *y*-direction is slightly more than that along the *z*-direction, whereas the distribution of "Z"-type along the *y*-direction is slightly less than that along the *z*-direction. This lateral deformation mechanism in tension was actually noticed by Xu *et al.*[18] for GOPFs and RGPFs, where the SEM images showed an obvious anisotropic tensile surface including fracture morphology even though the corresponding Poisson's ratios were not given. Notably, the anisotropic tensile Poisson's ratio behavior is also size-dependent to some degrees. The larger the GrF, the better the homogeneity. Therefore, it can be expected in the elastic range that the anisotropic effect of the tensile Poisson's ratios should be weakened (even to a large extent) when the sample is large enough to balance the distributions of "Z"-type and "N"-type in all the directions.

## Ductile Fracture Mode and Mechanism Near 45° Plane from Tensile Direction.

Unlike conventional counterparts, such as poly(ether imide) polymer with local pores,[25,26] closed-cell polymeric foam,[27] and open-cell nickel foam,[28] GrF has an obvious yielding plateau labeled as bc ($b'c'$) as shown in Figure 2a,b [the yield stress σ_y is at the point of $b(b')$]. This was also observed in GrF-PLC[10] and demonstrates that the specimen undergoes a large deformation with a relatively small increase in the applied load. Figure S2c,d shows that the deformation in the hardening stage cd ($c'd'$) is mainly viscoelastoplastic, where ~5.1% of viscous deformation was produced in holding, followed by 1.8% of plastic deformation, mainly from the yielding stage. As shown in the inset (b) of Figure 3, this plastic deformation from the yielding plateau can be further attributed to the rotation and slippage of the GrF flakes under shearing stresses, different from ductile metal materials such as low-carbon steel performed by grain boundary sliding along oblique surfaces.[29,30] Moreover, the flakes would rearrange once again near a 45° plane from the tensile direction labeled by a green line as shown in the inset (c) of Figure 3, and in this sense, the region mn ($m'n'$) in the hardening stage cd ($c'd'$) of Figure 2a,b can be viewed as a second yielding plateau. Figure 4 shows the distribution of normal stresses σ_{xx}
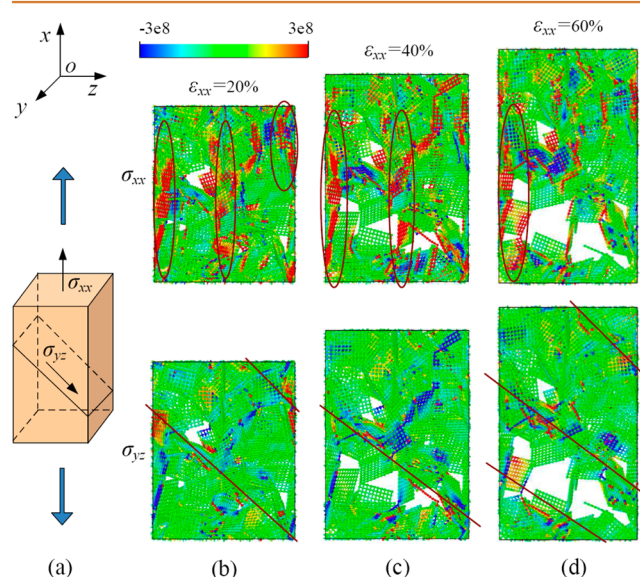
Figure 4. Stress distribution of 3D GrF in the tensile deformation. (a) Schematic diagram of the GrF sample in tension. Distribution of normal stresses σ_{xx} and shear stresses σ_{yz} in tensile strain of (b) 20%, (c) 40%, and (d) 60%, where the maximum values of σ_{xx} are circled by red ellipses, and the maximum values of σ_{yz} near a 45° plane from the tensile direction are labeled by red lines.

and shear stresses σ_{yz}. Figure 4b shows that shearing stresses σ_{yz} near a 45° plane are rather significant in the tensile strain $\varepsilon_{xx} = 20\%$, and they lead to slippage among GrF flakes, increasing the total normal strain and decreasing the average normal stress. In the top right corner of Figure 4b, the ~45° plane shearing stresses are also obvious, together with high local normal stresses, indicating that local instability occurs. In Figure 2a, a rapidly increasing total stress appears near the tensile strain $\varepsilon_{xx} = 20\%$, and a flake is torn open in shearing stresses and local normal stresses near a 45° plane, after a certain stress value of $\sigma_u = 110$ MPa has been reached (the strain is 22.15%), corresponding to the maximum load applied to the specimen
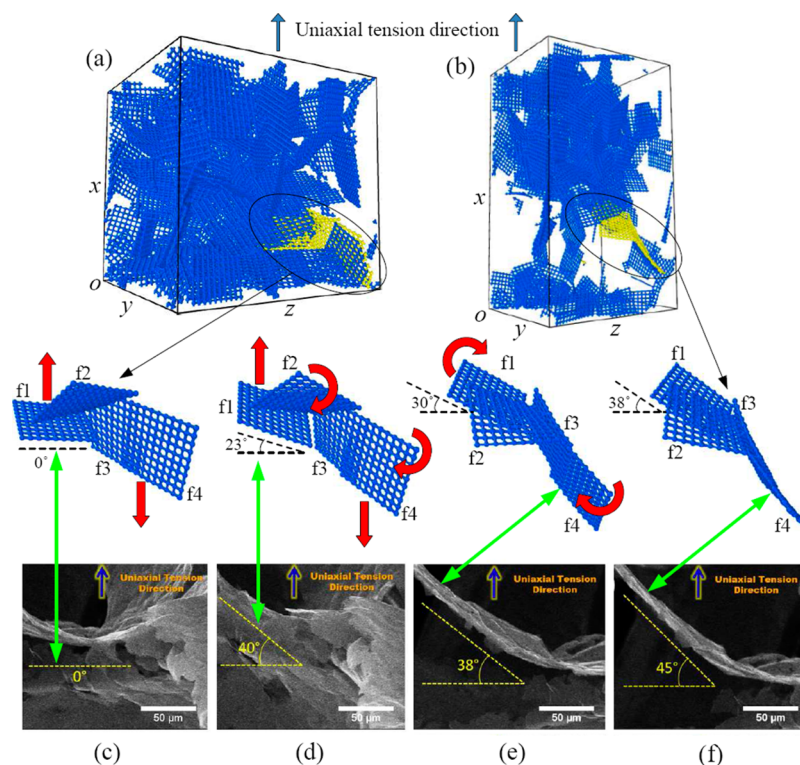
Figure 5. Evolution of mesostructure in tensile deformation. (a) Initial state and (b) final state of the GrF in uniaxial tension, where the local flakes considered are in yellow color. (c−f) Local mesostructures of four sequential thermodynamic states in the tensile deformation (see also Movie S2 in the Supporting Information for the dynamic process) and the corresponding SEM micrographs reproduced from Nieto *et al.*,[17] where f1−f4 indicate four constituent graphene flakes.

known as the ultimate strength. The local broken bonds are highlighted by the connected red atoms and green circle in inset (c) of Figure 3. For the GrF with a density of 5 mg/cm³, the tensile strength was 0.006 MPa,[17] but for the RGPFs with a density of ~71 mg/cm³, the tensile strength was ~11.2 MPa.[18] Hence, the tensile strength is also positively correlated to the density.

With the increase in the tensile deformation, the corresponding stress decreased until the rupture of the sample, and the corresponding stress, σ_b, at the point of $e(e')$ of Figure 2a,b, is known as the breaking strength. The entire dynamic process is shown in the Movie S1 of the Supporting Information, much better than the snap shots shown in Figure 3. Two main features different from conventional materials[25−29] can be observed from Figures 2a,b, 3, and 4 in the following:

(1) The stress decreases nonmonotonously with the tensile strain in the strain-softening stage of $de(d'e')$, with the feature of an obvious multipeak, labeled as p_I (p_I'), p_{II} (p_{II}'), and p_{III} (p_{III}') in Figure 2a,b. The GrF flakes would rearrange to hold continuing tensile deformation when the GrF sample comes into the softening stage. Because of the viscosity of the GrF, the movements and rearrangements of GrF flakes would lag behind the total deformation of axial direction, thus creating local stress concentrations in some flakes, as shown in Figure 4b,c for normal stresses circled by red ellipses. The SEM micrograph showed that a thin section of graphene branch bears a high stress;[17] furthermore, our simulation results in the insets (d−f) of Figure 3 show that the local bonds are broken near the peaks of p_I, p_{II}, and p_{III}. It is necessary to point out that, as a composite material, GrF

is comprised of a solid skeleton (graphene) and gaseous phase (air). According to Newnham's classification of diphasic composites,[31] the GrF has a 3-3 microstructure pattern. The graphene skeleton's formal geometry, which is governed by its connectivity, distributes the stress inside the composite, providing additional strength and residual stress reminiscent to a truss system used in structural engineering. Therefore, the number and magnitude of peaks or valleys are influenced by its formal geometry to some degree (Figure S2).

(2) Due to the multipeak tensile behaviors, the ductile fracture surface of GrF is not neat, and the corresponding morphology is shown in inset (g) of Figure 3, consistent with the experiment[17] directly reproduced in the inset (a) of Figure 3. Moreover, owing to the features of porous materials and layered crystals, the cross-link and vdW forces among GrF flakes are much smaller than the cohesive forces among molecules or atoms in ordinary materials such as poly(ether imide) polymer and low-carbon steel,[25,26,29] and the entire necking does not occur prior to the rupture, even though local graphene flakes contract themselves due to the intrinsic Poisson's ratio effect. The insets (a,g) of Figure 3 show that the fracture occurs at the 45° plane where the maximum stress, in the form of shear stress, rather than the normal stress shown in Figure 4, is experienced. Recalling the yield deformation in the maximum shear stress shown above, it can be concluded that the GrF, as a mechanical component, should be used within Tresca's hexagon.[29,30] Unlike metals, the fracture of the GrF does not start from a so-called "crack propagation", but performs in a form of breakable bead-bonds/linkages, as further disclosed.
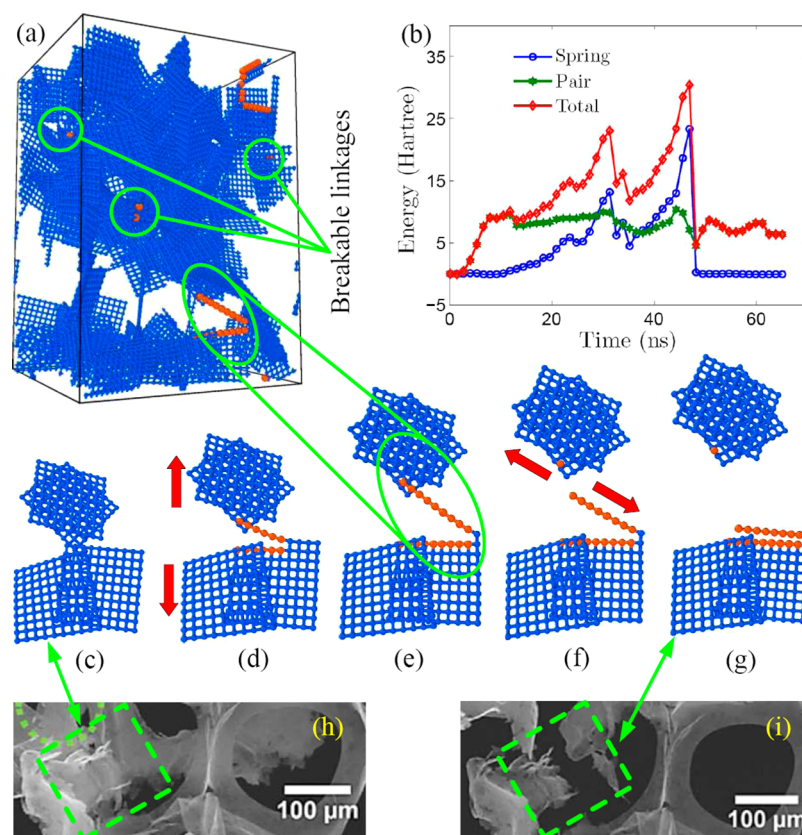
Figure 6. Tearing pattern of the flakes (with cross-links) in tensile deformation and the corresponding energy variation. (a) Global distribution of breakable bonds/linkages (in red for the connected atoms) in a certain uniaxial tensile state. (b) Variation in the energies with the loading time for the local broken bonds located in a certain graphene flake circled by green ellipse. (c–g) The snapshots of tearing pattern at five typical sequential evaluating dynamic states (see also Movie S3 in the Supporting Information for the entire process of tearing pattern). SEM micrographs reproduced from Nieto *et al.*[17] for (h) the initial state with discontinued graphene sheets and (i) the final state with ruptured graphene branches.

Evolution of Mesostructure and Local Rupture Mode.

Figure 5 shows the initial and final states of the tensile GrF and snapshots at four successive stages of the evolution of local mesostructure comprising four flakes labeled as f1, f2, f3, and f4. Initially, the entire sample is at a linear elastic state accompanying slight stretching for most flakes and local squeezing among some flakes. As the tensile strain increased, the squeezing and the resulting rippling fade away. After the flakes spread sufficiently, they started to move to align themselves along the vertical direction, as shown in Figure 5c, where flake f4 linking flake f3 moves down and flake f1 linking flake f2 moves slightly up. Owing to the cross-link and vdW forces, the above movements are accompanied by local turning of some flakes such as f2 and f4 plus f3, as shown in Figure 5d, which can be viewed as a part of the reason for the viscoelasticity. As also shown in Figure 5e, the turning of f2 makes the f2 hit against the fl, contributing to a part of the energy dissipation in tension with a slight fluttering. Subsequently, flake f1 slides on flake f2 and so do flakes f3 and f4 on other flakes near the 45° plane shown in Figure 5e, accompanying the residual fluttering in flake f2 and continuing the turning of link-flake f3–f4. The morphology shown in Figure 5f is formed in the final numerical foam of Figure 5b. The entire dynamic process was videotaped and is shown in Movie S2 in the Supporting Information. The video shows that the aligning of flake f1 is mainly towed by the down shifting and turning of f3–f4, consistent with the Supplementary video file

V1 shown by Nieto *et al.*[17] The considered graphene branch corresponds to f3 and f4, and the branch base corresponds to the f1 here. The matchups are mapped by green double arrow lines in Figure 5c–f. For the convenience of further quantitative comparison, we took f1 as an example to trace the angle between one of its sides and the horizontal line, and the resulting angle varies from 0° in Figure 5c to 38° in Figure 5f, withstanding the test of the SEM micrograph.[17] Additionally, the weak interior sliding within the GrF branch itself was not observed in the *in situ* SEM tensile testing,[17] indicating that the branch, as a multilayer graphene or a thin graphite, layers are held together stronger than different branches. In fact, Charlier *et al.*[32] used density functional theory (DFT) to study the relative contributions of vdW dispersive and "metallic" interactions. They found that a simple vdW model is not sufficient for an accurate description of interplanar bonding in graphite, where the contribution from vdW interactions only accounts for 8.4 meV/atom of the cohesive energy compared to the total energy of 20 meV/atom. The rest of the cohesive energy is provided by diverse "metallic" interactions that account for the interaction of electrons in one plane interacting with the ions and electrons in the neighboring planes of graphite. It is directly proved that the eight-layer graphene as a GrF flake in our model is rather reasonable.

To better understand the ductile fracture mode near the 45° plane from the vertical direction, Figure 6 directly shows the local evaluating rupture states and the variation in the energies

with loading time (neglecting the secondary kinetic energy). Figure 6b shows that the local energy variation can be decomposed into mesoscopic spring and pair harmonic potentials, and the severe energy fluctuation is mainly controlled by the former, partially by the latter. The spring potential leading to the fluctuation contributes to the local instability, causing the local rupture performed as the bonds break. This is the main reason for the multipeak tensile curve. Because there is no obvious stress concentration in small tensile strain, the flakes (with linkages) can hold their integrity, as shown in Figure 6c, but as the strain increased, the stress concentration became more apparent, as shown in Figure 6d. The left of the local mesostructure would hold larger stress than the right; therefore, the left bonds (together with the linkages) break at some dramatic moment, causing an opening tearing pattern in one GrF flake (a typical opening mode in fracture mechanics, a tensile stress normal to the plane of the crack).[30] The breakable bonds further accelerate the asymmetry of stress distribution, making more bonds break until the increase in the temporary balance shown in Figure 6e. On the other hand, owing to the shear stress, the local balance state cannot hold for a long time, and the broken bond-bead chain would be stretched nearby in the 45° plane from the vertical direction, as shown in Figure 6f, performing an in-plane shearing tearing pattern (a typical sliding mode in fracture mechanics, a shear stress acting parallel to the plane of the crack and perpendicular to the crack front).[30] The final broken mesostructure is clearly shown in Figure 6g. Furthermore, Figure 6h,i shows the SEM micrographs[17] of the initial state with discontinued graphene sheets and the final state with rupture graphene branches, respectively, corresponding well to those shown in Figure 6a,g, respectively. Such a local rupture analysis, in principle, can also explain cross-link breakings appearing in other positions in Figure 6a (see also the insets (c,e) in Figure 3 for those highlighted by the green circles and Figure S1), and the detailed dynamic process is supplied in Movie S3 of the Supporting Information. However, because of the good toughness from the viscoelasticity and viscoelastoplasticity of the GrF, as shown previously, the local breaking of bead-bonds/linkages cannot always occur or continue and sometimes stops or increasingly becomes more difficult, until the next stage where the local stress concentration appears again due to the increasing strain energy, or the mean stress is large enough so that another peak rises again in the stress−strain curve (Figure 2a,b).

CONCLUSION

In conclusion, utilizing physical cross-links and vdW forces acting among different graphene flakes by considering the resulting broken bead-bonds, a 2D mesoscopic graphene model was expanded into a 3D bonded GrF system for evaluating the uniaxial tensile behavior and fracture mode based on in situ SEM tensile testing. A multipeak stress−strain curve including its obvious yielding plateau and a ductile fracture near a 45° plane from the tensile direction including the surface morphology were both reproduced, and these phenomena can be reasonably explained by the corresponding stress distribution states. Both a power scaling law of effective modulus of elasticity with mass density and a slightly anisotropic strain-dependent Poisson's ratio were obtained. The mesoscopic physical and mechanical mechanisms of the tensile deformation were clearly elucidated by the evolution of mesostructure; moreover, the fracture feature and its thermodynamic states were directly navigated to the tearing

pattern of the mesoscopic graphene flake. This study would provide an effective way to elucidate the mesoscopic mechanisms for the highly interconnected integrated morphology of graphene branches and should contribute to multiscale computations of nano/meso/macromechanical performances and development of advanced graphene-based materials.

METHODS

Fabrication of 3D GrF Numerical Sample. As for preprocessing the initial GrF geometrical configuration, all the flakes with random normal vectors were placed in a huge cubic space lattice to ensure no mutual contact among them. Then, the NPT assemble technique with a constant temperature of 300 K and one barometric pressure (1 bar) was used to deal with the huge cubic numerical GrF system with a periodic boundary condition in three directions. As a result, the system shrank gradually and finally reached a pre-equilibrium state at ∼30 ns with a time step of 1 fs. Subsequently, by resetting the Berendsen barostat to 0 bar and the Langevin thermostat to 300 K, the system expanded slightly and reached the final equilibrium state at ∼500 ns with the criterion that the total energy fluctuation converges to <1%. The obtained final cubic numerical GrF sample with a length of ∼100 nm was filled by approximately uniform distributed flakes with an average mass density of ∼475 mg/cm^3, as shown in Figure 1c.

Uniaxial Tension in Strain-Controlled Loading. To gain an in-depth understanding of the multipeak stress−strain curve and ductile fracture near the 45° plane from tensile direction observed in experiments,[17] a series of uniaxial tensions in strain-controlled monotonic loading were conducted on our numerical model. Prior to the tensile simulations, 3D cross-links were added into the system among the neighboring graphene flakes at a distance of 2.5 nm, and the cross-linking positions were evenly distributed on edge-to-edge or/ and edge-to-surface or/and surface-to-surface,[21] as shown in Figure 1c. The static equilibrium of the GrF system with cross-links was achieved by the conjugate gradient method. The tensile strain rate was 10^7 s^{-1} along the x-direction (Figure 1c) at room temperature using a zero-pressure barostat in the other two directions, stretching the sample until fracturing with a time step of 1 fs.

Local (Position-Dependent) State of Stress. On the micro/ mesoscale, the virial stress can be viewed as a measure of the mechanical stress, even when simulating very inhomogeneous phenomena.[33] Based on a generalization of the virial theorem, the average virial stress over a volume Ω around a particle i at position r_i can be expressed as[34]

$$\sigma = \frac{1}{\Omega}\left(-m\frac{du_i}{dt} \otimes \frac{du_i}{dt} + \frac{1}{2}\sum_{j(\neq i)} r_{ij} \otimes f_{ij}\right) \tag{8}$$

where m is the mass of the particle in the GrF numerical sample and u_i is the displacement of i relative to the reference position; therefore, its material time derivative is the thermal excitation velocity of the particle. The interparticle force f_{ij} applied on particle i by particle j can be expressed as

$$f_{ij} = \frac{\partial \Phi_{ij}}{\partial r_{ij}}\frac{r_{ij}}{\|r_{ij}\|} \quad \text{with} \quad r_{ij} = r_i - r_j \tag{9}$$

where Φ_{ij} is the total energy of the coarse-grain ensemble considered, dating from the bead-spring and rotational-spring as well as pairwise interatomic potentials, as reported previously. The equivalence of the virial stress and Cauchy stress was reviewed by Subramaniyan and Sun using both theoretical arguments and numerical simulations.[35] All the simulations were implemented using an open-source software Large-scale Atomic/Molecular Massively Parallel Simulator (LAMMPS).[36]

ASSOCIATED CONTENT

Ⓢ Supporting Information

The Supporting Information is available free of charge on the ACS Publications website at DOI: 10.1021/acsnano.7b03474.

Movie S1: 3D numerical GrF sample during the tensile deformation (AVI)

Movie S2: Local evolution of mesostructure in 3D numerical GrF sample during the tensile deformation (AVI)

Movie S3: Tearing pattern of the mesoscopic graphene flake in 3D numerical GrF sample during the tensile deformation (AVI)

Force-field parameters, supplementary mechanical behaviors, further discussions, and datum extracted from related literatures (PDF)

AUTHOR INFORMATION

Corresponding Authors
*E-mail: tcwang@imech.ac.cn.
*E-mail: ygyao@bit.edu.cn.

ORCID
Douxing Pan: 0000-0002-9177-134X

Author Contributions
‖These authors contributed equally to the work.

Notes
The authors declare no competing financial interest.

REFERENCES

(1) Qiao, Z. H.; Tse, W.-K.; Jiang, H.; Yao, Y. G.; Niu, Q. Two-Dimensional Topological Insulator State and Topological Phase Transition in Bilayer Graphene. *Phys. Rev. Lett.* **2011**, *107*, 256801.

(2) Yang, W.; Chen, G. R.; Shi, Z. W.; Liu, C.-C.; Zhang, L. C.; Xie, G. B.; Cheng, M.; Wang, D. M.; Yang, R.; Shi, D. X.; Watanabe, K.; Taniguchi, T.; Yao, Y. G.; Zhang, Y. B.; Zhang, G. Y. Epitaxial Growth of Single-Domain Graphene on Hexagonal Boron Nitride. *Nat. Mater.* **2013**, *12*, 792−797.

(3) Ferrari, A. C.; Bonaccorso, F.; Fal'Ko, V.; Novoselov, K. S.; Roche, S.; Bøggild, P.; Borini, S.; Koppens, F. H. L.; Palermo, V.; Pugno, N.; Garrido, J. A.; Sordan, R.; Bianco, A.; Ballerini, L.; Prato, M.; Lidorikis, E.; Kivioja, J.; Marinelli, C.; Tapani Ryhänen, T.; Morpurgo, A.; et al. Science and Technology Roadmap for Graphene, Related Two-Dimensional Crystals, and Hybrid Systems. *Nanoscale* **2015**, *7*, 4598−4810.

(4) Lee, C.; Wei, X.; Kysar, J. W.; Hone, J. Measurement of the Elastic Properties and Intrinsic Strength of Monolayer Graphene. *Science* **2008**, *321*, 385−388.

(5) Chen, Z. P.; Ren, W. C.; Gao, L.; Liu, B. L.; Pei, S. F.; Cheng, H.-M. Three-Dimensional Flexible and Conductive Interconnected Graphene Networks Grown by Chemical Vapour Deposition. *Nat. Mater.* **2011**, *10*, 424−428.

(6) Han, S.; Wu, D. Q.; Li, S.; Zhang, F.; Feng, X. L. Porous Graphene Materials for Advanced Electrochemical Energy Storage and Conversion Devices. *Adv. Mater.* **2014**, *26*, 849−864.

(7) Xie, X.; Yu, G. H.; Liu, N.; Bao, Z. N.; Criddle, C. S.; Cui, Y. Graphene-Sponges As High-Performance Low-Cost Anodes for Microbial Fel Cells. *Energy Environ. Sci.* **2012**, *5*, 6862.

(8) Dasgupta, A.; Rajukumar, L. P.; Rotell, C.; Lei, Y.; Terrones, M. Covalent Three-Dimensional Networks of Graphene and Carbon Nanotubes: Synthesis and Environmental Applications. *Nano Today* **2017**, *12*, 116−135.

(9) Li, N.; Zhang, Q.; Gao, S.; Song, Q.; Huang, R.; Wang, L.; Liu, L. W.; Dai, J. W.; Tang, M. L.; Cheng, G. S. Three-Dimensional Graphene Foam As a Biocompatible and Conductive Scaffold for Neural Stem Cells. *Sci. Rep.* **2013**, *3*, 1604.

(10) Nieto, A.; Dua, R.; Zhang, C.; Boesl, B.; Ramaswamy, S.; Agarwal, A. Three Dimensional Graphene Foam/Polymer Hybrid as a High Strength Biocompatible Scaffold. *Adv. Funct. Mater.* **2015**, *25*, 3916−3924.

(11) Qiu, L.; Liu, J. Z.; Chang, S. L. Y.; Wu, Y.; Li, D. Biomimetic Superelastic Graphene-Based Cellular Monoliths. *Nat. Commun.* **2012**, *3*, 1241.

(12) Xu, Y.; Sheng, K.; Li, C.; Shi, G. Self-assembled Graphene Hydrogel *via* a Onestep Hydrothermal Process. *ACS Nano* **2010**, *4*, 4324−4330.

(13) Fang, Q. L.; Shen, Y.; Chen, B. L. Synthesis, Decoration and Properties of Three-Dimensional Graphene-Based Macrostructures: a Review. *Chem. Eng. J.* **2015**, *264*, 753−771.

(14) Wu, Y. P.; Yi, N. B.; Huang, L.; Zhang, T. F.; Fang, S. L.; Chang, H. C.; Li, N.; Oh, J.; Lee, J. A.; Kozlov, M.; Chipara, A. C.; Terrones, H.; Xiao, P. S.; Long, G. K.; Huang, Y.; Zhang, F.; Zhang, L.; Lepró, X.; Haines, C.; Lima, M. D.; et al. Three-Dimensionally Bonded Spongy Graphene Material with Super Compressive Elasticity and Near-Zero Poisson's Ratio. *Nat. Commun.* **2015**, *6*, 6141.

(15) Xu, X.; Zhang, Q.; Yu, Y.; Chen, W.; Hu, H.; Li, H. Naturally Dried Graphene Aerogels with Superelasticity and Tunable Poisson's Ratio. *Adv. Mater.* **2016**, *28*, 9223−9230.

(16) Nautiyal, P.; Boesl, B.; Agarwal, A. Harnessing Three Dimensional Anatomy of Graphene Foam to Induce Superior Damping in Hierarchical Polyimide Nanostructures. *Small* **2017**, *13*, 1603473.

(17) Nieto, A.; Boesl, B.; Agarwal, A. Multiscale Intrinsic Deformation Mechanisms of 3D Graphene Foam. *Carbon* **2015**, *85*, 299−308.

(18) Xu, Z.; Zhang, Y.; Li, P.; Gao, C. Strong, Conductive, Lightweight, Neat Graphene Aerogel Fibers with Aligned Pores. *ACS Nano* **2012**, *6*, 7103−7113.

(19) Peng, Q. Y.; Li, Y. B.; He, X. D.; Gui, X. C.; Shang, Y. Y.; Wang, C. H.; Wang, C.; Zhao, W. Q.; Du, S. Y.; Shi, E. Z.; Li, P. X.; Wu, D. H.; Cao, A. Y. Graphene Nanoribbon Aerogels Unzipped from Carbon Nanotube Sponges. *Adv. Mater.* **2014**, *26*, 3241−3247.

(20) Baimova, J.; Rysaeva, L. K.; Liu, B.; Dmitriev, S. V.; Zhou, K. From Flat Graphene to Bulk Carbon Nanostructures. *Phys. Status Solidi B* **2015**, *252*, 1502−1507.

(21) Wang, C.; Zhang, C.; Chen, S. The Microscopic Deformation Mechanism of 3D Graphene Foam Materials under Uniaxial Compression. *Carbon* **2016**, *109*, 666−672.

(22) Qin, Z.; Jung, G. S.; Kang, M. J.; Buehler, M. J. The Mechanics and Design of a Lightweight Three-Dimensional Graphene Assembly. *Sci. Adv.* **2017**, *3*, 1601536.

(23) Cranford, S.; Buehler, M. J. Twisted and Coiled Ultralong Multilayer Graphene Ribbons. *Modell. Simul. Mater. Sci. Eng.* **2011**, *19*, 054003.

(24) Chae, S. K.; Gunes, F.; Kim, K. K.; Kim, E. S.; Han, G. H.; Kim, S. M.; Shin, H.-J.; Yoon, S.-M.; Choi, J.-Y.; Park, M. H.; Yang, C. W.; Didier Pribat, D.; Lee, Y. H. Synthesis of Large-Area Graphene Layers on Poly-Nickel Substrate by Chemical Vapor Deposition: Wrinkle Formation. *Adv. Mater.* **2009**, *21*, 2328−2333.

(25) Pan, D. X.; Kang, G. Z.; Zhu, Z. W.; Liu, Y. J. Experimental Study on Uniaxial Time-Dependent Ratcheting of a Polyetherimide Polymer. *J. Zhejiang Univ., Sci., A* **2010**, *11*, 804−810.

(26) Pan, D. X.; Kang, G. Z.; Jiang, H. Viscoelastic Constitutive Model for Uniaxial Time-Dependent Ratcheting of Polyetherimide Polymer. *Polym. Eng. Sci.* **2012**, *52*, 1874−1881.

(27) Mills, N. J.; Zhu, H. X. The High Strain Compression of Closed-Cell Polymer Foams. *J. Mech. Phys. Solids* **1999**, *47*, 669−695.

(28) Aly, M. S. Tensile Properties of Open-Cell Nickel Foams. *Mater. Eng.* **2010**, *31*, 2237−2240.

(29) Kachanov, L. M. *Fundamentals of the Theory of Plasticity*; Dover Publications: Mineola, NY, 2004.

(30) Wang, T.-C.; Chen, S. H. *Advanced fracture mechanics*; Science Press, 2009.

(31) Newnham, R. E.; Skinner, D. P.; Cross, L. E. Connectivity and Piezoelectric-Pyroelectric Composites. *Mater. Res. Bull.* **1978**, *13*, 525−536.

(32) Charlier, J. C.; Gonze, X.; Michenaud, J. P. Graphite Interplanar Bonding: Electronic Delocalization and van der Waals Interaction. *Europhys. Lett.* **1994**, *28*, 403.

(33) Hardy, R. J. Formulas for Determining Local Properties in Molecular Dynamics Simulations: Shock Waves. *J. Chem. Phys.* **1982**, *76*, 622−628.

(34) Swenson, R. J. Comments on Virial Theorems for Bounded Systems. *Am. J. Phys.* **1983**, *51*, 940−942.

(35) Subramaniyan, A. K.; Sun, C. T. Continuum Interpretation of Virial Stress in Molecular Simulations. *Int. J. Solids Struct.* **2008**, *45*, 4340−4346.

(36) Plimpton, S. Fast Parallel Algorithms for Short-Range Molecular Dynamics. *J. Comput. Phys.* **1995**, *117*, 1−19.